Joint inversions of ground deformation, extrusion flux and gas emissions using physics-based models for the Mount St. Helens 2004-2008 eruption

Ying-Qi Wong [1], **and Paul Segall** [1]

[1]Department of Geophysics, Stanford University, Stanford, CA, USA

Key Points:

- Best-fit model produces satisfactory fits to all three datasets
- Elongate chambers of volume 64−256 km^3 with centroid at 9.0−17.2 km depth are preferred.
- Magma permeability, radius and friction are lower than estimates from inversions with the steady-state model.

Corresponding author: Ying-Qi Wong, `yqwong@stanford.edu`

Abstract

With the increasing quantity and quality of data collected at volcanoes, there is growing potential to incorporate all the data into analyses of the magmatic system. Physics-based models provide a natural and meaningful way to bring together real-time monitoring data and laboratory analyses of eruption products, at the same time improving our understanding of volcanic processes. We develop a framework for joint inversions of diverse time series data using the physics-based model for dome-forming eruptions from Wong and Segall (2019). Applying this method to the 2004-2008 eruption at Mount St. Helens, we estimate essential system parameters including chamber geometry, pressure, volatile content and material properties, from extruded volume, ground deformation and carbon dioxide emissions time series. The model parameter space is first sampled using the neighborhood search algorithm, then the resulting ensemble of models is resampled to generate posterior probability density functions on the parameters (Sambridge, 1999b, 1999a). We find models that fit all three datasets well. Posterior PDFs suggest an elongate chamber with aspect ratio less than 0.55, located at $9.0-17.2$ km depth. Since the model calculates pressure change during the eruption, we can constrain chamber volume to $64-256$ km^3. Volume loss in the chamber is $20-66$ million m^3. At the top of the chamber, total (dissolved and exsolved) water contents are $4.99-6.44$ wt% and total carbon dioxide contents are $1560-3891$ ppm, giving a porosity of 5.3-16.6% depending on the conduit length. Compared to previous inversions using a steady-state conduit model, we obtain a lower magma permeability scale, radius and friction coefficient.

Plain Language Summary

Data collected from volcanoes sheds light on the structure of the subsurface storage chamber and the migration of magma, thereby enhancing our understanding of volcanic hazards. Integrating multiple datasets into analyses of a single eruption can resolve more details of the volcanic system. A theoretical model that predicts these data given some input parameters is needed to connect diverse volcanological datasets. We have previously constructed a physics-based model that simulates the ascent of magma from the storage chamber to the surface through a pipe. The model is specialized for lava dome eruptions, such as the 2004-2008 at Mount St. Helens eruption, by taking into account magma solidification, gases coming out of solution and gases escaping from the system. The model is then used to calculate the lava dome volume, deformation of the land surface (detected by GPS) and rate of gas emissions. The model has several unknown parameters. We run many iterations of the model with different combinations of parameters and find models that fit all three datasets. This approach can constrain chamber geometry, pressure, gas content and material properties. Insights into this variety of system parameters would not have been possible with standard discipline-specific modeling.

1 Introduction

In the past few decades, the expansion of both ground and satellite-based monitoring systems, as well as advances in laboratory techniques to study volcanic products, have increased the quantity and quality of volcanological data. Since these observations are produced by common physical processes, physics-based models can provide a natural and meaningful way to bring together these diverse data, at the same time improving our understanding of volcanic processes.

A subset of models examines the last stages of magma's ascent through a volcanic conduit to the surface. These conduit flow models use fundamental conservation laws and rheologic models to simulate magma flow from chamber to surface. Phase changes affect magma properties such as density and viscosity which in turn regulate magma flux (e.g. Gonnermann & Manga, 2007). Models with varying levels of complexity have been developed to investigate the processes controlling effusive and explosive behavior, as well as to study both steady-state and time-varying conduit flow (e.g. Jaupart & Allègre, 1991; Denlinger & Hoblitt, 1999; Papale, 2001; Mastin, 2002; De' Michieli Vitturi et al., 2013). These studies have elucidated critical processes that determine eruption style and duration, such as the complex feedbacks between magma velocity and crystallization kinetics or gas escape that may produce cyclic lava discharge (Melnik & Sparks, 2005; Kozono & Koyaguchi, 2012). Connections to observations mainly involve qualitative comparisons between observed and predicted magma flux, which is a direct model output. A few studies have gone further to couple conduit models to the surrounding crust to compare with observed ground deformation (e.g. Albino et al., 2011; Anderson & Segall, 2011; Kawaguchi & Nishimura, 2015; Neuberg et al., 2018).

Prior work by Anderson and Segall (2013) demonstrated the utility of physics-based volcanic models in joint inversions of geophysical datasets. Their study focused on eruptions that produce a lava dome at the surface. The 1D model simulates ascent of a three-phase magma, taking into account gas solubility and its effect on viscosity. Ascending magma causes the pressure in the chamber to drop, decreasing flow velocity exponentially in time. Model outputs were compared with extruded volume and geodetic data from the 2004-2008 eruption at Mount St. Helens using the Markov Chain Monte Carlo (MCMC) algorithm. Since conduit models can be highly non-linear, this probabilistic approach captures the range of model parameters consistent with the observations. Compared with traditional geodetic inversions, incorporating the physics-based model with extruded volume data allowed more parameters to be constrained, including initial chamber pressure, dissolved volatile content, and magma and chamber compressibility. The physics-based model is the crucial link that ties these datasets together.

In order to harness the full power of joint inversions using physics-based models, we need to capture the essential physical processes in the magmatic system. For dome-forming eruptions, slow ascent allows magma to crystallize gradually, an effect greatly simplified in the model of Anderson and Segall (2013). Gases exsolving during ascent may escape from the magma, which, together with crystallization, is critical to forming dense, degassed plugs in the shallow reaches of conduits (e.g. Kozono & Koyaguchi, 2012; Schneider et al., 2012). Wong et al. (2017) developed a steady-state physics-based model which incorporated crystallization and gas escape to study the quasi-steady phase of the 2004-2008 Mount St. Helens eruption, when magma flux was approximately constant. Diverse data, including magma flux, dome rock porosity, solidus depth and plug depth, were used to derive distributions on critical system parameters. Wong and Segall (2019) extended this conduit model to study the temporal evolution of conduit flow. Scaling analysis showed that when chamber pressure declines slowly relative to the magma ascent rate such as in dome-forming eruptions, steady-state solutions are inadequate in modeling the initial decline in magma flux, therefore requiring time-dependent solutions. Qualitative comparisons with extruded volume, ground deformation and gas emissions time series identified the most influential system parameters.

In this study, we develop a framework for quantitative joint inversions of diverse time series datasets using the time-dependent conduit flow model from Wong and Segall (2019). Given extrusion volume, ground deformation and carbon dioxide emissions time series from the 2004-2008 Mount St. Helens eruption, we estimate essential system properties including chamber geometry, initial pressure, volatile content and material properties. A suitable inversion technique for physics-based models should account for the non-linearity of volcanic systems, therefore we prefer probabilistic methods that estimate not only an optimal solution but also the range of admissible solutions (?, ?). At the same time, since the model is computationally expensive, we are unable to use simple stochastic methods such as MCMC that require millions of forward model evaluations. Based on these considerations, we choose to apply the Neighborhood Algorithm which is trivially parallelizable and can build probability density functions (PDFs) of the relevant system parameters (Sambridge, 1999b, 1999a).

2 Methods

2.1 Physics-based model for Mount St. Helens plumbing system

We have developed a physics-based model of the plumbing system at Mount St. Helens to simulate magma ascent from an ellipsoidal magma chamber through a conduit to the surface (Figure 1). The model is one-dimensional (radially-averaged). Properties in the chamber are taken as lumped parameters evolving with time, while properties in the conduit are modeled in both time and depth. In this section, we present a brief overview of the chamber-conduit model; details can be found in Wong and Segall (2019).

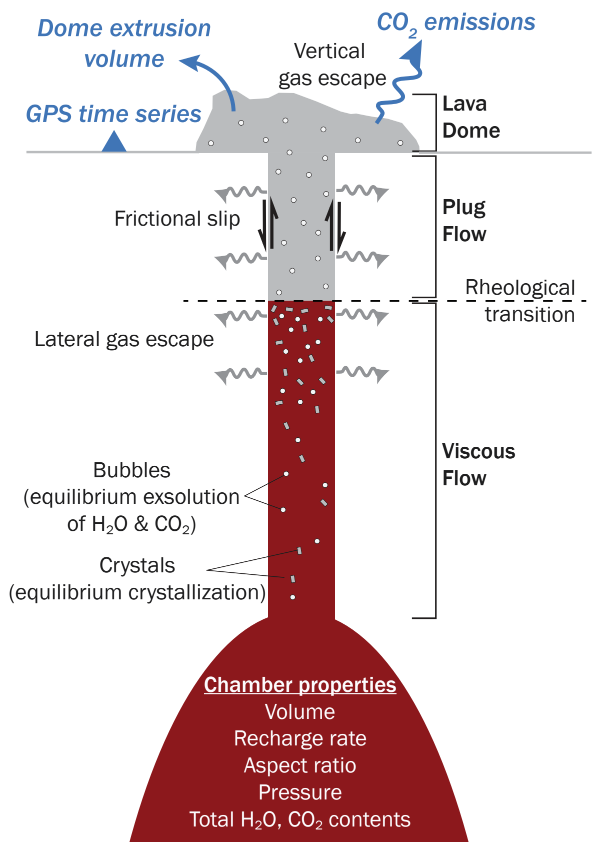

Figure 1. Model setup, adapted from Wong and Segall (2019). Magma ascends viscously from a chamber through a cylindrical conduit, where it undergoes crystallization, gas exsolution and gas escape, eventually transitioning to a solid plug that slides along the conduit walls. The three datasets used to constrain model parameters are shown in blue.

At the beginning of the eruption, pressure in the chamber exceeds the magma column weight and drives flow out of the chamber towards the surface. The ascending magma exsolves volatiles and crystallizes. Once enough volatiles exsolve, the gas volume fraction exceeds the percolation threshold and permits gases to escape from the system both vertically through the conduit and laterally through the conduit walls. The combined effects of gas exsolution, gas escape and crystallization strongly influence viscosity and cause the magma flow regime to evolve naturally from viscous flow at depth to solid plug sliding in the shallow part of the conduit. Removal of magma from the chamber lowers the chamber volume and pressure over time, which decreases the magma ascent velocity asymptotically towards zero.

2.1.1 Conduit flow model

Magma consists of solids, liquid melt which contains dissolved water (H_2O) and carbon dioxide (CO_2), as well as exsolved volatiles, giving its density ρ as

$$\rho = \rho_s\phi_s + \rho_l\phi_l c_1 + \rho_g\phi_g \tag{1}$$

For each phase, the density and volume fraction are ρ and ϕ respectively. Subscripts indicate the phase: s for solids, l for liquid melt, and g for gases. The term c_1 accounts for dissolved volatiles and depends on the dissolved mass concentrations of H_2O and CO_2 (χ_h^d, χ_c^d), which are modeled as functions of pressure and temperature using the solubility relations from Liu et al. (2005). We derive the solid volume fraction ϕ_s by assuming isothermal equilibrium crystallization of the water-saturated Mount St. Helens dacite (Pallister et al., 2008; Schneider et al., 2012).

These component phases affect magma viscosity η, which is a combination of the melt viscosity η_m and the relative viscosity increase due to solids η_s,

$$\eta = \eta_m(\chi_h^d, \chi_c^d, T)\ \eta_s(\phi_s, \dot{\gamma}), \tag{2}$$

We apply the dacite melt viscosity model of Whittington et al. (2009), which depends on dissolved volatile content and temperature T. For the relative viscosity increase due to solids, we apply the model of Costa (2005) and Caricchi et al. (2007) which incorporates a dependence on strain rate $\dot{\gamma}$. The effect of bubbles on viscosity is neglected since porosity of the 2005 Mount St. Helens dome lavas is relatively low, thus the effect of crystals predominates (Llewellin & Manga, 2005).

Applying these magma properties, the governing equations for 1D conduit flow are

$$v = v_{\text{visc}} + v_{\text{fric}} = \frac{\tau_R R}{4\eta} + 2v_r \exp\left(-\frac{f_0}{a}\right)\sinh\left(\frac{\tau_R}{a\sigma_c}\right), \quad \text{where} \tau_R = -\frac{R}{2}\left(\frac{\partial p}{\partial z} + \rho g\right) \tag{3}$$

$$\frac{\partial}{\partial t}(\rho_s\phi_s + \rho_l\phi_l) = -\frac{\partial}{\partial z}[(\rho_s\phi_s + \rho_l\phi_l)v] \tag{4}$$

$$\frac{\partial}{\partial t}\left(\chi_h^d\rho_l\phi_l c_1 + \frac{1}{1+\Gamma}\rho_g\phi_g\right) = -\frac{\partial}{\partial z}\left[\left(\chi_h^d\rho_l\phi_l c_1 + \frac{1}{1+\Gamma}\rho_g\phi_g\right)v + \frac{1}{1+\Gamma}\rho_g\phi_g(v_g - v)\right] - \frac{2\rho_g\phi_g u_g}{R(1+\Gamma)} \tag{5}$$

$$\frac{\partial}{\partial t}\left(\chi_c^d\rho_l\phi_l c_1 + \frac{\Gamma}{1+\Gamma}\rho_g\phi_g\right) = -\frac{\partial}{\partial z}\left[\left(\chi_c^d\rho_l\phi_l c_1 + \frac{\Gamma}{1+\Gamma}\rho_g\phi_g\right)v + \frac{\Gamma}{1+\Gamma}\rho_g\phi_g(v_g - v)\right] - \frac{2\Gamma\rho_g\phi_g u_g}{R(1+\Gamma)} \tag{6}$$

The radially-averaged momentum balance (equation 3) gives magma velocity v as a combination of incompressible, steady, laminar Poiseuille Flow v_{visc} and a rate-dependent frictional slip boundary condition v_{fric} (Rice et al., 2001) (full derivation in Wong and Segall (2019)). Flow is driven by the difference between the vertical pressure gradient $\partial p/\partial z$ and the gravitational load ρg, giving shear stress τ_R. The conduit has constant radius R. The conduit walls have depth-dependent effective normal stress $\sigma_c(z)$, which is the difference between lithostatic normal stress and hydrostatic pore pressure, $(\rho_{\text{lith}} - \rho_{\text{hyd}})gz$, neglecting tectonic and topographic contributions. Wall friction is parameterized by the nominal coefficient f_0, rate-dependence a, and reference velocity v_r. Deep in the conduit, where η is low and σ_c is high, v_{visc} predominates and magma flows viscously. In the shallower conduit, magma solidification increases η while σ_c decreases, increasing v_{fric} until frictional sliding becomes the dominant flow regime.

Continuity for solids and liquids (equation 4) reflects the exchange of mass as liquid melt solidifies during ascent. Continuity for H_2O (equation 5) contains both dissolved and exsolved components. Transient mass changes are balanced by the flux of volatiles as well as vertical and lateral gas flow out of the conduit at gas velocities v_g and u_g respectively (e.g. Kozono & Koyaguchi, 2012; Schneider et al., 2012). The term $\Gamma = (1-$

$m_h)\mathcal{M}_c/(m_h\mathcal{M}_h)$ is the mass ratio of exsolved CO_2 to H_2O, where m_h is the mole fraction of water in the vapor phase and $\mathcal{M}_c, \mathcal{M}_h$ are the molar masses of CO_2 and H_2O respectively. A similar form describes the continuity of CO_2 (equation 6).

To model gas escape from the system, we apply Darcy's Law while assuming chemical and mechanical equilibrium between the gas phase and the ambient melt (Jaupart & Allègre, 1991; Schneider et al., 2012; Kozono & Koyaguchi, 2012). This implies that gas and melt pressures are the same. The gas velocities are given by

$$(v_g - v) = \frac{k_{\text{mag}}}{\eta_g}\frac{\partial p}{\partial z} \tag{7}$$

$$u_g = \frac{k_{\text{lat}}}{\eta_g}\frac{p - p_{\text{hyd}}}{2R}, \tag{8}$$

where η_g is the gas viscosity, and $p_{\text{hyd}} = \rho_{\text{hyd}} g z$ is the hydrostatic pressure. In vertical gas escape, gas flows through the magma only, thus the permeability constant in equation 7 is the magma permeability k_{mag} modeled using the Carman-Kozeny relation,

$$k_{\text{mag}} = k_c \phi_g^3,\ \phi_g > \phi_{gc}, \tag{9}$$

where k_c is a scaling constant, ϕ_g is the gas volume fraction (porosity) and ϕ_{gc} is the percolation threshold, which is the minimum porosity to form interconnected pathways and has a typical value of $\sim 30\%$ (Klug & Cashman, 1996; Saar & Manga, 1999; Blower, 2001). In lateral gas escape, gas flows through both magma and the wall rock. The lateral permeability k_{lat} is a harmonic average of k_{mag} and the crustal permeability model from Manning and Ingebritsen (1999).

2.1.2 Boundary and initial conditions

Taking into account the constitutive relations, the model solves for four field variables at each depth and time: pressure, velocity, gas volume fraction (porosity) and mole fraction of water in the vapor phase, compiled into the vector $y(z,t) = [p, v, \phi_g, m_h](z,t)$. The governing equations provide $4(N_z - 1)$ equations, where N_z is the number of depth points. This system of equations requires 4 boundary conditions to be complete: pressure and volatile contents in the chamber, and pressure at the top of the conduit.

At the beginning of the eruption, chamber pressure is greater than the magma column weight to drive flow. As the eruption proceeds, magma outflux causes the chamber pressure to decrease, while influx from a deeper source may increase the chamber pressure (e.g. Segall, 2013),

$$\frac{dp_{\text{ch}}}{dt} = \frac{q_{\text{in}} - q_{\text{out}}}{\rho_0 V_0(\beta_{\text{mag}} + \beta_{\text{ch}})} = \frac{\Omega(p_{\text{deep}} - p_{\text{ch}}) - \pi R^2 v_{\text{ch}}}{V_0(\beta_{\text{mag}} + \beta_{\text{ch}})}, \tag{10}$$

where Ω is a proportionality constant linking recharge in the chamber to the magmastatic head between the chamber and a deep reservoir at pressure p_{deep}, v_{ch} is the velocity at the conduit base, V_0 is the initial chamber volume, while β_{mag} and β_{ch} are the magma and chamber compressibilities respectively,

$$\beta_{\text{mag}} = \frac{1}{\rho}\frac{\partial \rho}{\partial p}, \quad \beta_{\text{ch}} = \frac{1}{V}\frac{\partial V}{\partial p}, \tag{11}$$

where ρ, p are evaluated at the center of the chamber (Anderson & Segall, 2011). Magma density in the chamber is calculated using equation 1, while chamber center pressure is the sum of pressure at the conduit inlet and magmastatic head from the chamber top to center. Chamber compressibility is estimated from the numerical results for different ellipsoidal chamber shapes (Amoruso & Crescentini, 2009). Scaling analysis of equation 10 with equations 4–6 shows that if the ascent timescale is much shorter than the chamber pressure evolution, the time-dependent model should approximate steady-state solutions evaluated at the identical chamber pressure (Wong & Segall, 2019). This could occur if the chamber volume is large ($>$ 1000 km^3). On the other hand, if the ascent and chamber pressure evolution timescales are comparable, full time-dependent solutions are needed to model conduit flow.

Other boundary conditions are the H_2O and CO_2 mass concentrations in the chamber χ_h^{ch}, χ_c^{ch}. Using the solubility equations, the volatiles are separated into dissolved and exsolved components to determine the gas volume fraction and mole fraction of water to carbon dioxide at the base of the conduit. Finally, the pressure at the conduit exit is assumed to be atmospheric pressure.

We initialize the model with the steady-state solution given specified boundary conditions at $t = 0$ using the code from Wong et al. (2017). Natural eruptions clearly do not start from steady-state, and future work is needed to derive more realistic eruption onsets that simulate acceleration of partially solidified conduit magma leftover from lava dome eruptions in the 1980s.

2.1.3 Model parameters and prior bounds

To solve each forward model, we specify magma chamber properties (aspect ratio, volume), conduit geometry (length, radius), material properties (magma permeability scale, conduit wall friction), and conduit base boundary conditions (initial pressure, volatile contents). In this study, we set the recharge rate Ω to zero because the extruded volume time series appears to flatten out at the end of the eruption, suggesting that there is no recharge. Previous inversions also suggest that syn-eruptive recharge is minor (Anderson & Segall, 2013). Sensitivity analyses showed that the observations are insensitive to percolation threshold, thus we fix it to the typical value of 30% (Wong & Segall, 2019). The chamber depth is uniquely determined from the chamber volume, aspect ratio and conduit length. For a consistent description of the initial conduit base pressure for different conduit lengths, the total pressure at the conduit base p_{ch} is defined in terms of an excess pressure Δp_0 at $t = 0$,

$$p_{\mathrm{ch}}(t = 0) = p_{\mathrm{atm}} + \rho_l g L + \Delta p_0, \tag{12}$$

where p_{atm} is the pressure at the top of the conduit and ρ_l is the melt phase density. We choose a wide range for the model parameter prior bounds to minimize the influence of prior assumptions on the posterior probabilities (Table 1).

2.2 Data from the 2004-2008 Mount St. Helens eruption

The 2004-2008 Mount St. Helens eruption began with swarms of shallow volcano-tectonic earthquakes on September 23, 2004 that culminated in a series of explosions starting on October 1, 2004 (Moran et al., 2008; Scott et al., 2008). These explosions gave way to lava extrusion under the crater glacier, forming a large welt on the south side of the 1980s lava domes (Vallance et al., 2008; Scott et al., 2008; Dzurisin et al., 2015). The new lava eventually broke through the glacier and was first seen on October 11, 2004. Thereafter, a series of lava spines, some of which resembled "whalebacks", were extruded on the crater floor. Extrusion was accompanied by tilt cycles (Vallance et al., 2008; Anderson et al., 2010) and repetitive low-frequency and hybrid "drumbeat" earthquakes that were suggested to be caused by stick-slip motion of a solid plug ascending through the conduit (Moran et al., 2008; Iverson, 2008). After 3.3 years, eruptive activity waned and finally ended in January 2008 (Dzurisin et al., 2015).

During the eruption, a wide variety of data was collected. Three time series datasets were chosen to compare with model predictions: (a) extruded volume which indicates the evolution of exit velocity, (b) gas emissions which inform us about volatile content and permeability, and (c) ground deformation which reflects pressure change and geometry of the magma reservoir. We also include constraints on the porosity of magma exiting the conduit.

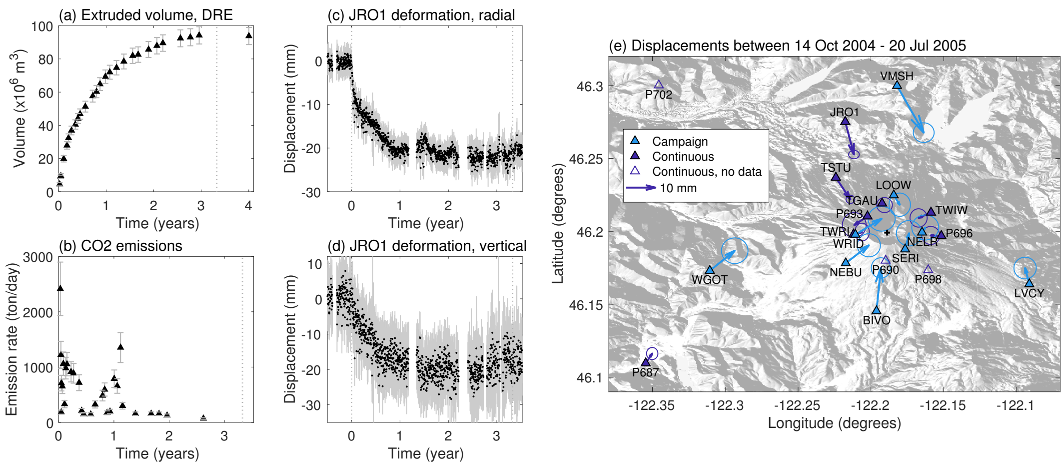

Figure 2. Datasets from the 2004-2008 Mount St. Helens eruption used in this study: (a) Dense rock equivalent (DRE) time series of extruded volume. (b) Carbon dioxide emission rates. (c-d) Radial and vertical deformation at 14 continuous GPS stations were used, here showing, as an example, JRO1, the only nearby station in operation at the eruption onset. (e) Map view of stations within 20 km of the volcano with displacement vectors between two campaigns during the eruption (14 October 2004 – 20 July 2005). Another 2 stations (KELS and P421) are outside this map view. Light blue filled triangles are campaign stations, dark blue filled triangles are continuous stations in operation during this period, and dark blue open triangles are continuous stations that started operation after 14 October 2004. Black cross denotes the center of the crater.

2.2.1 Extruded volume

Differential Digital Elevation Models (DEMs) using aerial photogrammetry tracked the growth of the lava dome in the crater (Schilling et al., 2008; Dzurisin et al., 2015) (Figure 2a). In the initial few weeks of the eruption, lava was extruded beneath the crater glacier, precluding direct observation of dome growth. Deformation of the glacier surface showed a welt of approximately 10±1 million m^3 by October 11, 2004. After that, lava broke the surface of the glacier and direct observations of the lava dome growth became possible to generate the widely-used time series of dome volume change. The total extruded volume reached a maximum of 94.2 million m^3, while uncertainties in these volume estimates are $\sim$ 4%. Post-eruption volume decline is attributed to dome compaction. From this data, we remove an estimated dome porosity of 10% to obtain the dense rock equivalent (DRE) volume (Cashman et al., 2008; Smith et al., 2011).

From the model predictions, we calculate the DRE extruded volume from the extrusion rate by excluding the gas volume fraction and integrating over time (Anderson & Segall, 2011),

$$V_{\text{ex}}(t) = \pi R^2 \int_0^t v(z=0,t)[1-\phi_g(z=0,t)]\,dt, \tag{13}$$

We compare the predicted and observed extruded volume time series to assess model fit. We additionally impose a constraint that the increase in extruded volume over the final two measurements, recorded at 3.0 and 4.0 years after the eruption start, is small (i.e. less than 4×10^6 m^3, the average error in the extruded volume measurements) to ensure that the final extrusion flux is approximately zero.

2.2.2 Carbon dioxide emissions

During the eruption, emissions of carbon dioxide generally decayed with time. These data, along with measurements of sulfur dioxide and hydrogen sulfide, were collected via aircraft sampling of the vapor plume (Gerlach et al., 2008) (Figure 2b). Gases escaping both vertically through the conduit and laterally through the wall rocks may be observed at the surface. However, in calculating the gas flux at the surface, we approximate that all CO_2 in the plug escaped vertically. Laboratory measurements of permeability indicate that vertical permeability is much higher than lateral permeability (Gaunt et al., 2014). In addition, we would expect a time lag in gas emissions if lateral gas percolation was important. This delay was not observed: emissions decayed below the detection threshold before the end of the eruption. Model predictions thus serve as an upper bound on vertical gas escape. We calculate the carbon dioxide emissions as

$$Q_c^{ex}(t) = \pi R^2 \frac{\Gamma}{1+\Gamma} \rho_g \phi_g (v_g - v)\bigg|_{z=0}, \tag{14}$$

where all variables are evaluated at the surface. Note that there is also flux of gas transported within pores in the magma, however, this contribution is small since v is much smaller than $(v_g - v)$ at the surface.

2.2.3 Ground deformation from GPS stations

The eruption was monitored by a network of continuous and campaign Global Positioning System (GPS) stations around the volcano (Figure 2c-e). Most of these stations were installed after the eruption began. Only one station, JRO1 at the Johnston Ridge Observatory, captured the eruption onset, which was characterized by rapid deflationary motion of about 10 mm in two weeks (Lisowski et al., 2008; Anderson & Segall, 2013).

To obtain the volcanic deformation signal, we downloaded and processed position time series from continuous GPS stations in the USGS Pacific Northwest Network, focusing on stations within 100 km of Mount St. Helens. Stations on Mount Rainier were omitted due to strong measurement drift due to snow. The region around Mount St. Helens experiences long-term deformation due to convergence of the North American and Juan de Fuca plates, slow slip events, seasonal fluctuations and volcano-related deformation. We first identify slow slip time intervals between 1999 and 2020 using the relative strength index (Crowell et al., 2016) on 36 stations located between 20 and 100 km of the volcano. A slow slip event must be identified by at least two stations in order to be accepted. Next, we simultaneously estimated tectonic deformation rates, slow slip offsets, sinusoidal seasonal effects and amplitudes for power law noise including white, flicker and random walk using the Maximum Likelihood Estimation (MLE) approach (Mao et al., 1999; Langbein, 2004; Williams, 2008) on the post-eruption position time series (2012–2020) which has no discernible volcanic deformation. We assume that tectonic deformation, seasonal variability and noise amplitudes are the same before and after 2012. We remove the tectonic deformation and seasonal signal from the whole time series, and apply the noise amplitudes to the covariance matrix of syn-eruptive measurements. Offsets due to slow slip events and antenna maintenance before 2012 were removed by taking averages before and after the offset. The result is the deformation due to volcanic activity.

Of the GPS stations within 100 km of Mount St. Helens, 21 are within 60 km of the volcano and recorded displacements during the eruption period. 8 of these 21 continuous stations only recorded the latter half of the eruption when deformation was limited and thus were excluded from the inversions. For the remaining 13 stations, the covariance matrix for the deformation time series was modeled using amplitudes obtained in the MLE and uncertainties in the tectonic velocity and SSE offset estimates. Note that data during slow slip events were removed from the data, causing gaps in the time series, because we do not model the time-dependent deformation caused by these events.

Additional campaign GPS measurements from 9 stations between October 14, 2004 and July 20, 2005 were incorporated. This time period spans 0.05 to 0.8 years after eruption onset. Based on the continuous station data, this period encapsulates a large proportion of the total deformation. These campaign measurements can therefore provide additional constraints on chamber geometry and depth. Tectonic velocities at the continuous GPS stations were linearly interpolated (i.e. assuming constant plate strain and rotation rate) to remove tectonic velocities at the campaign GPS stations. Slow slip offsets and seasonal fluctuations were ignored due to lack of constraints, which may bias the campaign displacements. In particular, vertical deformation at nearby, high elevation stations had high errors.

From the model-predicted pressure decay time series, we calculate radial displacements using the expressions of Yang et al. (1988) for prolate spheroidal chambers. We do not consider the effect of conduit tractions on surface displacements, because the GPS stations are far from the vent relative to the plug length.

2.2.4 Additional constraint on magma porosity

As an additional inversion constraint, we considered the porosity of dome lava specimens collected by helicopter (Pallister et al., 2008; Thornber et al., 2008). These specimens consist of dense, light-gray dacite with porosities below 10% and vesicular, dark gray to red dacite with porosities of 25–40% (Cashman et al., 2008). One helium pycnometer measurement indicated a connected porosity of 30.4% (Cashman et al., 2008). Five intact samples with no deformation textures showed porosity declining from 19.7% to 10.3% after two years (Smith et al., 2011). Applying the porosity time series from Smith et al. (2011) directly to the inversion is challenging because of the small number of samples and the fact that they consist of intact, centimeter to meter scale samples which may or may not be representative of the average porosity across the tens-of-meter scale conduit. Therefore we opt for a simple constraint that admits only models whose predicted porosity time series is entirely less than the maximum observed porosity of 40%.

2.3 Inversions using the neighborhood algorithm

We apply the neighborhood algorithm (Sambridge, 1999b, 1999a) to estimate critical properties of the Mount St. Helens plumbing system. Previous studies have applied this algorithm to volcano deformation to determine the location and volume change of magma chambers, as well as to model dike geometry from InSAR data (e.g. Pritchard & Simons, 2002; Fukushima et al., 2005). The neighborhood algorithm consists of two stages: (1) the model space search and (2) the ensemble appraisal.

2.3.1 Searching the model space

Stage 1 generates an ensemble of models by searching the model space to find models that have high posterior probabilities (Sambridge, 1999b). This stage is akin to an adaptive grid search. In this section, we first define the posterior probability and then describe the search algorithm.

The posterior probability $p(\mathbf{m}|\mathbf{d})$ of each model is

$$p(\mathbf{m}|\mathbf{d}) \propto L(\mathbf{d}|\mathbf{m})p(\mathbf{m}) \tag{15}$$

where $L(\mathbf{d}|\mathbf{m})$ is the data likelihood and $p(\mathbf{m})$ is the prior probability distribution. In this study, we assume uniform priors on the model parameters, however this inversion scheme can be easily adjusted to incorporate other priors. Uniform priors have constant

$p(\mathbf{m})$ while $\mathbf{m}$ is within pre-defined bounds. The posterior probability therefore depends only on the likelihood,

$$L(\mathbf{d}|\mathbf{m}) \propto \exp\left[-\frac{1}{2}\frac{1}{\sum_k w_k}\Phi\right], \tag{16}$$

$$\text{where}\Phi = \sum_k \left[w_k(\mathbf{d}_k - \hat{\mathbf{d}}_k)^T \Sigma_k^{-1}(\mathbf{d}_k - \hat{\mathbf{d}}_k)\right], \tag{17}$$

where k denotes the dataset (extruded volume, continuous GPS positions, campaign GPS displacements, CO_2 emissions) and Φ is the joint misfit to the data. For the kth dataset, w_k is the weight, $\mathbf{d}_k$ are the observed data, $\hat{\mathbf{d}}_k$ are the predicted data, and Σ_k is the covariance matrix.

The simplest joint misfit is obtained by assigning equal weights ($w_k = 1$) for all k datasets. However, initial tests show that this approach does not find well-fitting solutions to this problem because of the high scatter in the CO_2 emissions. This scatter arises from unmodeled processes (e.g. crack propagation in the plug that allows sudden release of gases) or measurement errors (e.g. wind dispersal of emissions) that cannot be captured by the current physics-based model, which can only predict smoothly decaying solutions. Therefore we need to reduce the weight of the CO_2 emissions w_{CO2} to prevent the misfit to the CO_2 emissions from dominating the total misfit. To determine w_{CO2}, we bin the emissions into months and examine the variability among measurements in the same month (Figure 3). During the 2.6-year observation duration, eight months had more than one observation (months 0, 1, 2, 3, 5, 10, 11, 13). In these eight months, the root-mean-square deviation from the monthly average ranged from 12 – 597 ton/day. Normalizing the high estimate of 597 ton/day by the median measurement error of 97 ton/day gives a scale factor of 6.15. Therefore we assign w_{CO2} as the reciprocal of the square of this scale factor to get units of variance, giving $w_{\mathrm{CO2}} = 1/(6.15^2) = 0.0264$. Weights to all other datasets were assigned as 1.

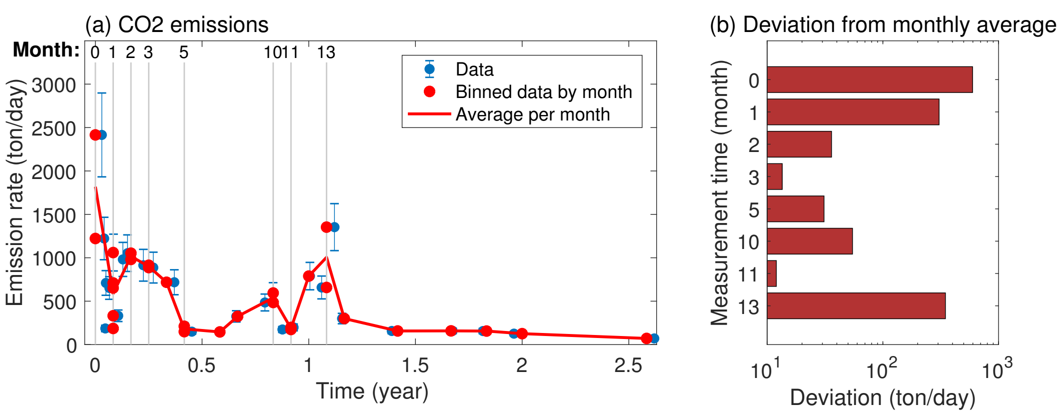

Figure 3. Determining the weight for the CO_2 emissions time series. (a) Observed emissions (blue dots with error bars) and binned by month (red dots). Red line tracks the average for each month. Months with more than one observation are indicated at the top of the axis. (b) Root-mean-square of deviations of observed CO_2 emissions from the monthly average for the 8 months that had multiple observations.

The search algorithm in the Stage I is as follows: first, N_s model parameter combinations are randomly chosen to run the forward model and evaluate the joint misfit (equation 17). The forward model evaluations can be run in parallel. From this set of models, the best-fitting N_r models, where $N_r \leq N_s$, are selected for the next iteration. Since we use uniform priors, finding models that minimize the misfit is equivalent to maximizing the posterior probability. In the next iteration, a new set of N_s/N_r models is generated in the neighborhood of each selected model. As an example, if $N_s = 200, N_r = 100$, the 100 best-fitting models are chosen at this stage, and 2 new points are generated in the neighborhood of each of these 100 models to generate a total of 200 new points. The "neighborhood" is defined using Voronoi cells, where cell boundaries are the midpoint of two models. Sambridge (1999b) provides an efficient method to calculate these cell boundaries. The misfits of each of these new models are then evaluated, and the process of selecting well-fitting cells and generating new models and misfits is repeated until the minimum misfit approaches a constant.

The neighborhood search is simple to implement and only requires two tuning parameters N_s, N_r which influence the effectiveness of the model space search. Large N_s, N_r produce a more exploratory search; small N_s, N_r improve the algorithm's capability as an optimizer although it may become susceptible to local minima.

2.3.2 Appraising the ensemble of models

Stage 2 resamples the ensemble of models using a Gibbs Sampler to generate probability density functions (PDFs) of the model parameters (Sambridge, 1999a). Within the neighborhood of each model, the posterior probability $p(\mathbf{m}|\mathbf{d})$ is assumed to be constant, so that no new forward model runs are required. Starting from a high probability model, the Gibbs Sampler takes a random step along each parameter axis in turn according to the conditional probability along the current axis $p(m_j|\mathbf{m}_{-j}, \mathbf{d})$ (the probability of parameter m_j given all other specified parameters $\mathbf{m}_{-j}$). Following Sambridge (1999a), we generate this random step using the rejection method: first, a uniform random deviate m_j^{prop} is generated within the specified model parameter bounds. The proposed step is then compared with the maximum probability along that axis and another uniform random deviate r on the interval (0,1). The proposed step is accepted if

$$\log r \leq \log p(m_j^{\text{prop}}|\mathbf{m}_{-j}, \mathbf{d}) - \log p(m_j^{\max}|\mathbf{m}_{-j}, \mathbf{d}). \tag{18}$$

If m_j^{prop} is rejected, this procedure is repeated until a step is accepted. This procedure is repeated for each parameter axis, and then on subsequent samples. The rejection method only compares the log probabilities between two models and does not require calculation of the actual probabilities, thereby avoiding numerical underflow issues.

Two input parameters are needed for the Gibbs sampler: the length of each Gibbs sampling chain, and the number of chains. We test different values for these two parameters until the PDFs converge. In this study, a general rule is that the chain length should be at least 2000 and at least 50 chains should be sampled.

3 Results

3.1 The model parameter space

For Stage 1 of the neighborhood algorithm, we run the algorithm with $N_s = N_r = 200$ for 600 iterations, which was sufficient for model parameters to converge and for maximum model likelihoods to reach a stable value (Figure 4). Parameters for the maximum likelihood model lie well within the prescribed bounds. After 20 iterations, we reduced the lower bound of conduit radius from 20 m to 10 m as the best fit model appeared to be very close to 20 m. Chamber aspect ratio and volume appear to converge after about 400 iterations. Other parameters converge more slowly, eventually reaching a stable maximum likelihood model (red line, parameters in Table 1). During the search, the algorithm also explored a region distinct from the global maximum likelihood (pink line in Figure 4). On closer inspection, we observe that these models have non-smooth solutions caused by a slight numerical instability at the percolation threshold. Smoothing the percolation threshold transition removes this instability, but the predicted data for these

Table 1. Model parameters with their prior bounds, best-fit values from the neighborhood search, as well as the median model and 90% credible interval from the neighborhood appraisal.

Symbol	Description	Prior bounds	Best-fit from search	Median model	90% credible interval
Chamber properties					
α	Aspect ratio (width/height)	$0.05 - 1$	0.30	0.36	$0.13 - 0.55$
V_0	Volume (km^3)	$10 - 500$	130	136	$64.1 - 256$
Ω	Recharge rate (m^3 day^{-1} Pa^{-1})	0 (fixed)			
Conduit geometry					
L	Length (km)	$2 - 8$	4.55	4.75	$2.95 - 5.79$
R	Radius (m)	$10 - 100$	20.6	22.1	$11.9 - 35.8$
Material properties					
k_c	Magma permeability scale (m^2)	$10^{-20} - 10^{-10}$	$10^{-13.5}$	$10^{-13.5}$	$10^{-14.7} - 10^{-12.1}$
ϕ_{gc}	Percolation threshold	$0.2 - 0.4$	0.25	0.25	$0.21 - 0.28$
f_0	Nominal coefficient of friction	$0.01 - 0.8$	$10^{-1.66}$	$10^{-1.66}$	$10^{-1.94} - 10^{-1.26}$
a	Rate-dependence of friction	$10^{-3} - 10^{-1}$	$10^{-2.69}$	$10^{-2.77}$	$10^{-2.97} - 10^{-2.37}$
Conduit base boundary conditions					
Δp_0	Excess pressure at $t = 0$ (MPa)	$5 - 50$	18.9	18.9	$11.6 - 26.3$
χ_h^{ch}	Total water content (wt%)	$3 - 7$	5.55	5.73	$4.99 - 6.44$
χ_c^{ch}	Total carbon dioxide content (ppm)	$100 - 5000$	2925	2802	$1560 - 3891$

models produce poor fits to the observations. In particular, these solutions fail to satisfy the zero flux condition at the end of the eruption. Therefore we reject these non-smooth solutions as unphysical.

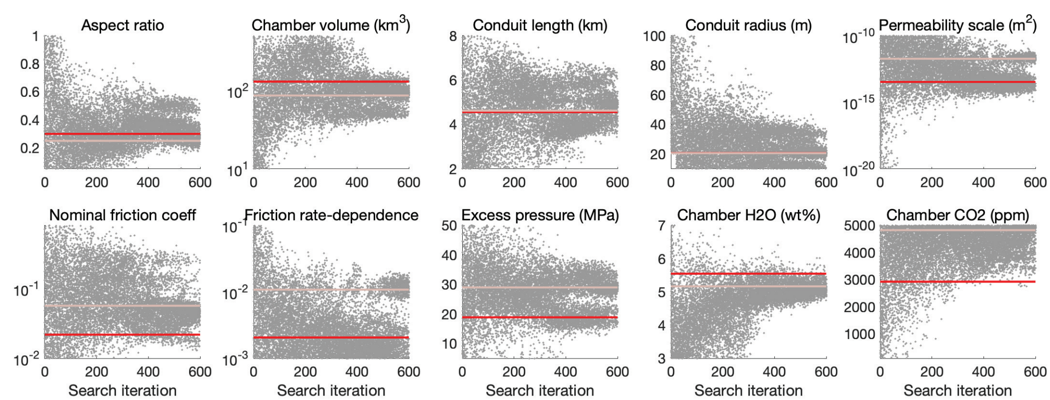

Figure 4. Model parameters at each neighborhood search iteration. Model parameter bounds are the limits of the vertical axis. Red line marks the best-fit model. Pink line marks one model with non-smooth solutions.

This ensemble of models produces reasonable fits to the combined dataset (Figure 5). Predicted extruded volume from the best-fit model to the combined dataset (red line) matches early observations well, but underpredicts the data at later times because of the higher measurement error. Similarly, the models accepted in the appraisal step (pink envelope) closely follow early volume estimates but show a wider range of final extruded volume. The predicted JRO1 radial displacement follows the observations well. Due to the lower weight applied to the CO_2 emissions time series, the pink envelope spans a wide range, broadly capturing the decreasing trend and range of values.

Predicted radial displacements between 14 October 2004 and 20 July 2005 mostly follow the observations, particularly at the continuous GPS stations (Figure 5d(ii)). Ra-

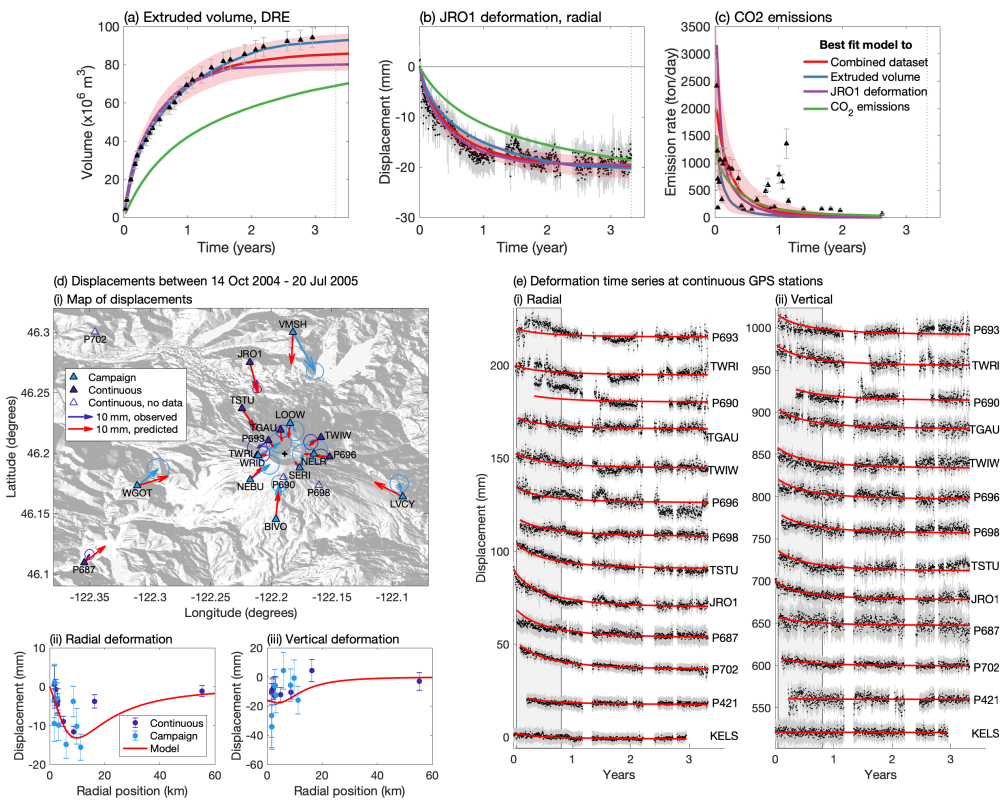

Figure 5. Best-fit model to the combined dataset (red line) compared to observations. (a) Extruded volume, (b) JRO1 radial displacement and (c) CO_2 emissions time series. For (a-c), the range of the models accepted in the appraisal step (pink area), as well as the best-fit models to individual datasets are also shown. Vertical gray dotted lines indicate the eruption end. (d) Predicted displacements from the best-fit model to the combined dataset, showing the (i) map, (ii) radial displacements and (iii) vertical displacements as functions of radial distance from the crater. (e) Predicted radial and vertical deformation time series at the continuous GPS stations, ordered by closest (P693) to furthest (KELS) from the crater. Vertical gray rectangle indicates the time period of the two campaigns. Gaps in the time series occur during slow slip events.

dial displacements at the campaign stations are noisier but follow the same general trend. Fits to vertical deformation during this time are poorer. Campaign stations WRID, NELR and SERI experienced large vertical displacements (light blue points between −20 and −40 mm in Figure 5d(iii)) that are likely caused by seasonal effects such as snow accumulation because these stations are at high elevation. The rest of the vertical deformation data suggest that the maximum should be offset from the crater center (where radius is zero), supporting a prolate ellipsoid model for the chamber (Yang et al., 1988). This same model also fits the deformation time series at the continuous GPS stations.

Compared to the best-fit models to individual datasets, the best 1000 models to the combined dataset cannot match each observation as well (Figure 5a-c). Some penalization of fit is needed. For example, the best-fit model to the JRO1 deformation (purple line) better captures the initial rapid deflation which flattens out after 1 year. However, this trend yields poor fits to the observed extruded volume both in magnitude and temporal trend. In order to simultaneously fit the GPS and extruded volume time series, the search finds models that have slightly poorer fit to the initial rapid deflation at JRO1. Similarly, the best-fit model to the combined dataset has a distinctively different trend compared to the best-fit model to the CO_2 emissions (green line), which produces a significantly poorer fit to the other datasets.

3.2 Posterior probabilities of model parameters

We appraise the ensemble of models to generate posterior probability density functions (PDFs) of the model parameters by converting misfits to likelihoods (equation 16, Figure 6). For comparison, we also calculate the likelihoods given only extruded volume, only deformation, and the combination of extruded volume and deformation from the ensemble, and appraise the result. For these appraisals, we also apply the constraints on dome porosity and zero final extrusion flux.

In general, when more datasets are used, the marginal posterior PDFs show tighter constraints on the model parameters as expected. The extruded volume time series constrains the chamber volume, conduit radius, nominal friction coefficient, excess pressure, magma permeability scale and total volatile contents (Figure 6a). Total extruded volume scales as $(\beta_{\mathrm{mag}}+\beta_{\mathrm{ch}})\Delta p_{\mathrm{ch}} V_0$ (Segall, 2013) and therefore can offer constraints on chamber volume given estimates on compressibility which depends on the exsolved volatile content. The extrusion rate can help to constrain the exsolved volatile content, as a higher exsolved volatile content would decrease bulk density and enable faster magma ascent. However, this relationship may not be unique as the extrusion rate is also affected by the driving pressure, rate of gas escape and frictional resistance.

Deformation data alone improves constraints on chamber properties (aspect ratio, volume, conduit length which controls chamber centroid depth, excess pressure), but volatile content and frictional properties are poorly constrained (Figure 6b). When extruded volume and deformation are jointly analyzed, the distributions on all the model parameters except the frictional properties become narrower (Figure 6c). This estimation is enhanced by inclusion of CO_2 emissions data in the appraisal. Naturally, the distribution on chamber CO_2 content is tighter and slightly lower than estimated in the other three appraisals. This lower volatile content may explain the slightly lower nominal friction coefficient: a decrease in magma buoyancy requires a corresponding decrease in flow resistance.

In all four ensemble appraisals, the magma permeability scale is well constrained to be above 10^{-16} m^2, with all four distributions having approximately similar widths. This indicates that dome porosity data, which is common to all four appraisals, is the main control on magma permeability scale. In order for the dome porosity to remain under 40%, magma permeability has to be high enough to allow volatiles to escape from the conduit.

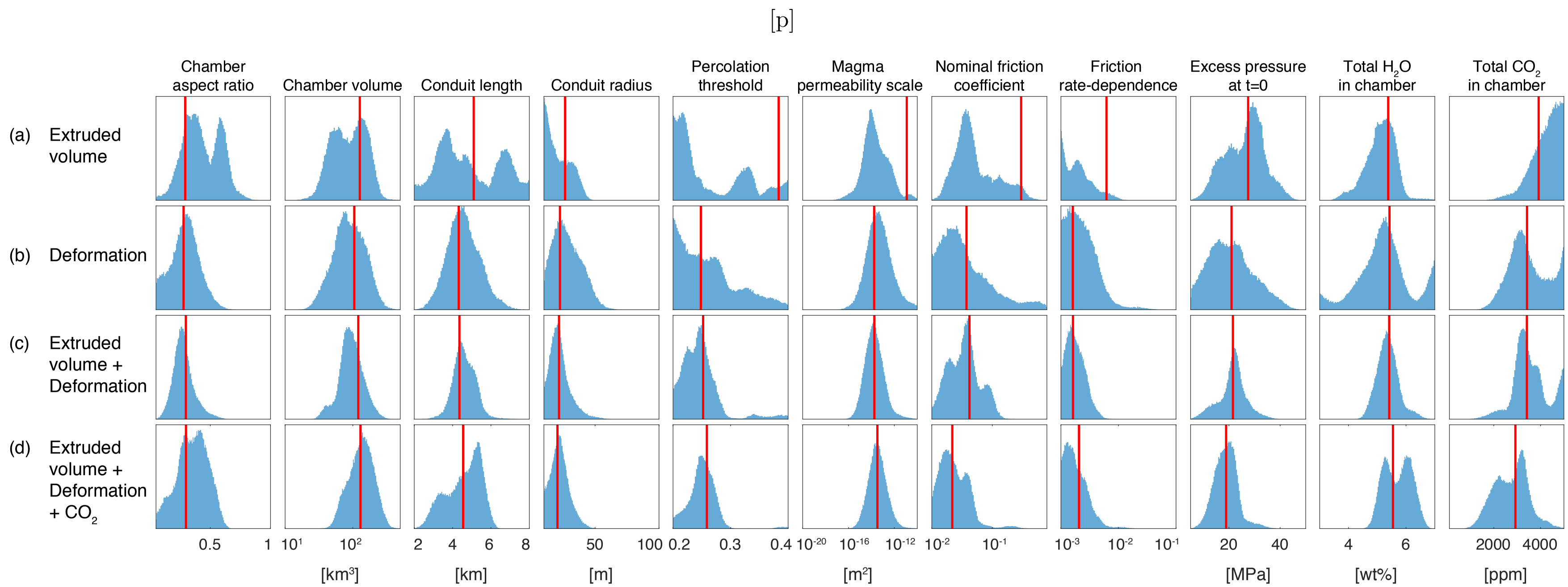

Figure 6. Marginal posterior PDFs of the model parameters when the appraisal is constrained by different datasets. Top row uses extruded volume time series only; middle row uses continuous and campaign GPS data, while the bottom row uses all datasets. Limits of the horizontal axis correspond to the bounds of the uniform prior. Vertical red lines denote the highest likelihood models for each appraisal.

In the following sections, we analyze the results of the appraisal by looking at subsets of parameters. Any quoted ranges of parameter values are the 90% credible intervals of the posterior PDF.

3.2.1 Chamber properties

The preferred chamber volume lies between 64.1−256 km^3 (Figure 7a), well below the threshold that indicates that the chamber evolution timescale is comparable to the ascent timescale. This implies that steady-state solutions are poor approximations to the temporal evolution of the system, which requires the full time-dependent governing equations (Wong & Segall, 2019). The data prefer an elongate chamber with an aspect ratio (width/height) of 0.13−0.55 with its top (equivalent to conduit length) located at 2.95−5.79 km depth. The chamber centroid is located at 9.00−17.2 km depth with the semi-major axis estimated as 4.59−14.0 km. These parameters indicate that most chambers lie between 5−20 km depth and span about 2 km in width (Figure 7b).

The chamber geometry parameters are highly correlated. Aspect ratio exhibits a negative correlation with the semi-major axis because of how they affect the chamber volume: a more elongate chamber requires a longer axis to occupy the same volume. A more elongate chamber also has to be located deeper. Volume loss in the chamber, which ranges between 20.0 and 66.2$\times$10^6 m^3, exhibits a positive correlation with volume and centroid depth. Pressure at the conduit base ranges from 80.6−144.4 MPa and is highly correlated with conduit length to ensure that magma can be pushed out of the conduit at a similar velocity. This corresponds to $13.1 - 55.5$ MPa over magmastatic pressure (weight of magma column) needed to overcome viscous losses and frictional resistance. Porosity at the conduit base not only depends on the total water content (not shown), but also the conduit length and pressure at the base of the conduit.

3.2.2 Volatiles and permeability

Volatile contents in the chamber are well-constrained in the appraisal (Figure 8a, b). Total H_2O contents of $4.99 - 6.44$ wt% and CO_2 contents of $1560 - 3891$ ppm are preferred. These volatile contents are partitioned into dissolved and exsolved components. Dissolved H_2O encompasses the relatively common 3.34−4.65 wt% for arc magmas (Plank et al., 2013), while dissolved CO_2 is estimated to be 22.0−100.3 ppm. Together, these imply a substantial exsolved phase occupying $5.3 - 16.6$% volume fraction at the base of the conduit. This corresponds to a magma compressibility of 0.20−2.67$\times$10^{-10} Pa^{-1}. Chamber compressibility, which depends on the shape of the chamber and elastic modulus of the crust (here 20 GPa), has a very narrow range, thus magma compressibility largely controls the total compressibility which ranges from $0.69 - 3.09 \times 10^{-10}$ Pa^{-1}.

The exsolved phase may be lost through permeable gas escape, both vertically through the conduit column and laterally through the conduit walls. The magma permeability scale is well constrained at 1.84$\times$10^{-15}−7.23$\times$10^{-13} m^2, and the percolation threshold is 0.21−0.28. Vertical gas escape only depends on the magma permeability and ranges between $8.20 \times 10^{-18} - 2.36 \times 10^{-15}$ m^2. Lateral gas escape depends on the magma and wall-rock permeability. However, at the percolation threshold, wall rock permeability spans a narrow range of 1.08−2.21$\times$10^{-15} m^2 and is generally higher than magma permeability. Magma permeability is thus the limiting factor for lateral gas escape. This causes the distribution for both permeabilities to be approximately equal.

3.2.3 Conduit friction

Extruded volume is the main control on conduit friction due to its relationship with extrusion rate (Figure 6). In contrast, ensemble appraisal using only the deformation dataset produces broader distributions on both frictional parameters. When combining extruded

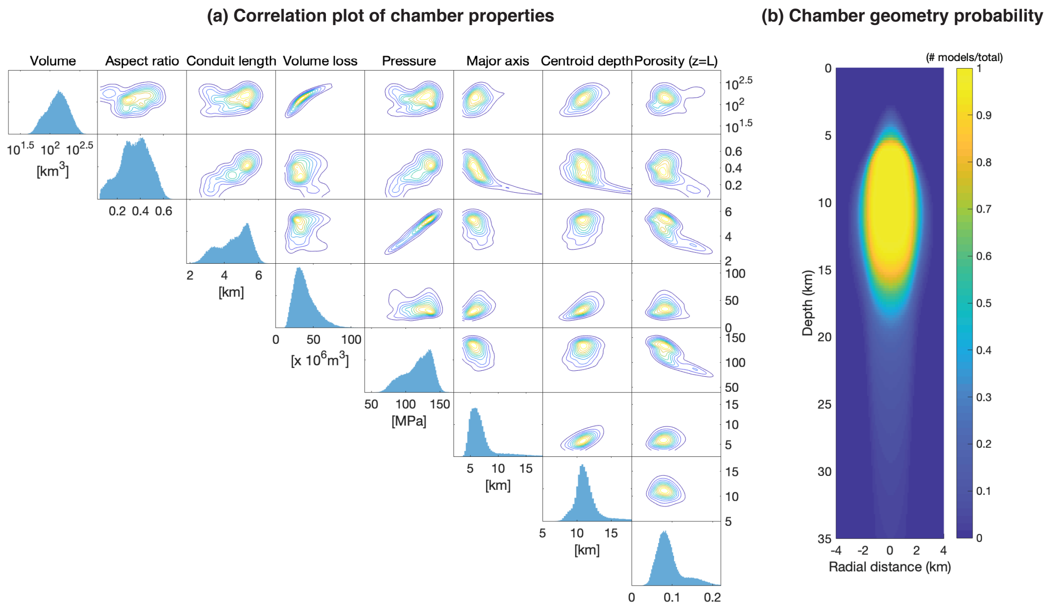

Figure 7. Chamber properties constrained in the appraisal that considers the likelihood of all the datasets. (a) Correlation plot of the chamber properties. Volume, aspect ratio and conduit length are directly estimated, while volume loss, pressure (measured at the chamber top), semi-major axis, centroid depth and porosity (measured at the chamber top) are dependent parameters. (b) 2D slice of the crust showing the probability of finding a chamber at a certain depth and radial distance from the Mount St. Helens edifice. Colors indicate the number of models relative to the total.

volume and deformation data, posterior probabilities of friction become narrower. Since predicted gas emissions depend on the pressure gradient in the plug which is affected by frictional resistance, the ensemble appraisal with all datasets results in a well-constrained nominal frictional coefficient. The marginal posterior PDFs suggest that the nominal friction coefficient is low ($10^{-1.94} - 10^{-1.26}$), while the rate-dependence of friction ranges between $10^{-2.97}$–$10^{-2.37}$. This corresponds to friction coefficients between 0.014–0.057 at the reference velocity $v = v_r = 10^{-5}$ m/s (Figure 9). Shear stress is given by $f\sigma_c$ where σ_c is the effective normal stress. At the plug depth (0.76–0.96 km), shear stress ranges between $0.23 - 0.82$ MPa.

4 Discussion

Traditional geodetic inversions have used continuous and campaign GPS data from the Mount St. Helens 2004 - 2008 eruption to constrain the geometry and volume change of the chamber (Lisowski et al., 2008; Palano et al., 2012). Using a source model of three colocated orthogonal point cracks, Lisowski et al. (2008) obtain a chamber with an aspect ratio of 0.66 centered at 7.99 km depth with a volume change of 11.9 million m^3 in the first year of eruption. Applying the Yang et al. (1988) model for ellipsoidal chambers, Palano et al. (2012) found a more elongated chamber with aspect ratio 0.10 at a similar depth with a volume change of 7.97 million m^3 in the first two years of the eruption. Notably, the discrepancy in aspect ratio between the two studies arises from the difference in source model, as the predicted spatial pattern of deformation are approximately the same in both studies.

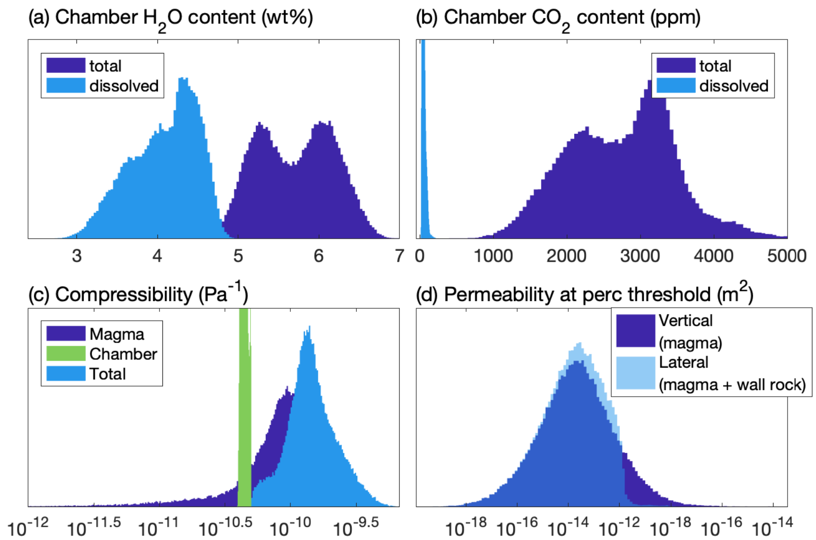

Figure 8. Posterior PDFs of (a) total and dissolved H_2O content in the chamber, (b) total and dissolved CO_2 content in the chamber (note low dissolved content), (c) magma compressibility in the chamber and the chamber compressibility, and (d) vertical and lateral permeability at the percolation threshold depth.

In this study, we applied the source model from Yang et al. (1988) as it satisfies the free surface boundary condition and, in the limit where the chamber is deep relative to the chamber dimensions, the pressure boundary condition on the chamber walls. Therefore our results align more closely with Palano et al. (2012) to prefer a more elongate chamber. The highest likelihood chamber has an aspect ratio of 0.30 with a volume change of 35.8 million m^3 over the whole eruption. The chamber centroid is located at 11.2 km depth. The volume change estimated in this inversion is about 3–4 times larger than Lisowski et al. (2008) and Palano et al. (2012) respectively due to both the longer time interval considered and also the deeper centroid location (Figure 7a). The top of the chamber, located at 4.55 km, has a pressure of 121.4 MPa. This agrees with petrologic constraints, which find that plagioclase phenocrysts continued to grow until pressure decreased to 130 MPa (corresponding to 5 km depth) when magma exits the chamber and enters the conduit (?, ?; Pallister et al., 2008).

Incorporating a physics-based model and extrusion volume data enables us to resolve pressure change and chamber volume, which traditional geodetic inversions are unable to do. Athough Palano et al. (2012) obtained a plausible volume change, their preferred model has a pressure change of 1000 MPa and a chamber of volume of only 0.306 km^3. This large pressure change is inconsistent with the tensile strength of rock which is on the order of 10 MPa. Using a physics-based model with extrusion flux and deformation data, (Anderson & Segall, 2013) modeled a pressure change of $2-10$ MPa over the course of the eruption. Combined with the volume change of $16-40$ million m^3 constrained by deformation, they estimate the chamber to be at least 40 km^3 and reaching the upper bound of the inversion at 200 km^3. In this study, the 90% credible interval of the resampled models have pressure change 2-18 MPa and volume loss $16-40$ million m^3, implying a chamber volume of 64-256 km^3. Total extruded volume scales as $(\beta_{\rm mag}+\beta_{\rm ch})\Delta p_{\rm ch} V_0$ (Segall, 2013). Given the final extrusion volume of 94.2 million m^3 and typical system compressibility of $0.69-3.09\times10^{-10}$ Pa^{-1}, this implies a chamber volume on the order of 10^2 km^3, consistent with our posterior PDFs. A similar analysis in Mastin

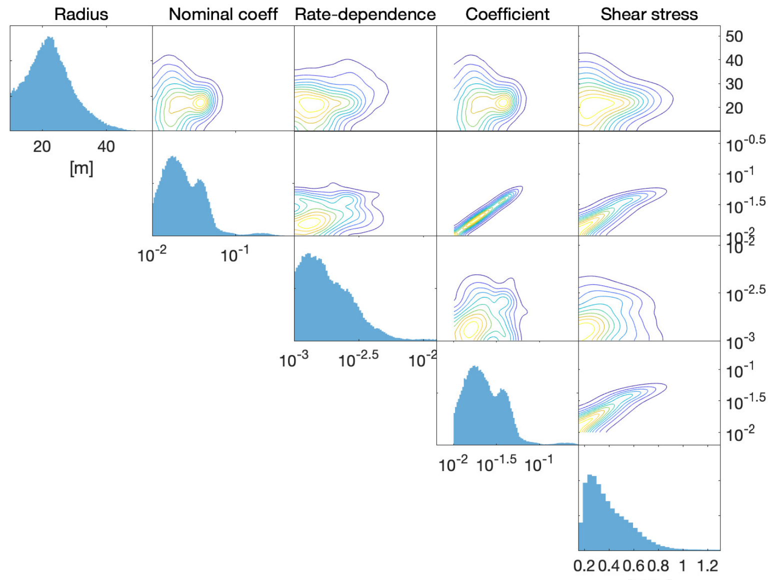

Figure 9. Correlation plots of frictional parameters. Conduit radius, nominal coefficient and rate-dependence are directly estimated, while the friction coefficient at the reference velocity $v = v_r = 10^{-5}$ m/s and shear stress are dependent parameters.

et al. (2009) obtained a smaller chamber volume estimate of $10-25$ km^3 by using a similar pressure change but $4-5$ times higher magma compressibility. This difference in compressibility arises because Mastin et al. (2009) used a fixed crystal volume in the chamber, while we include the increase in density due to crystallization, which counteracts some of the decrease in density caused by gas exsolution and expansion. As a result, compressibilities obtained in this study are smaller.

Independent estimates of chamber volume at Mount St. Helens span a wide range from a few km^3 to 1000 km^3. Eruption volumes can offer a lower bound on chamber size. The largest plinian eruption in the Holocene produced 4 km^3 of material (Carey et al., 1995). However, given that Mount St. Helens has more frequently produced lava flows and domes, the more common eruption volume is smaller (Clynne et al., 2008; Pallister et al., 2017). Earthquake hypocenters in the 1980s show distinct lobes surrounding an earthquake-free zone, thought to be the semi-liquid magma body, of about $10-20$ km^3 (Scandone & Malone, 1985). Recent seismic tomography in the iMUSH experiment found a body with low shear wave velocities at $4-13$ km depth and spanning 15 km wide, corresponding to a volume 1000 km^3 (Kiser et al., 2016). Our inversions agree with the vertical extent of the chamber but suggest a more limited horizontal extent. This volume is an upper bound due to resolution limitations. In addition, the melt fraction causing the reduction in shear wave velocities is uncertain. Petrologic evidence of compositionally diverse magma batches with different stagnation depths suggests that volume estimated the iMUSH experiment may reflect a mush containing distinct regions of high melt fraction (Leeman & Smith, 2018; Wanke, Clynne, et al., 2019; Wanke, Karakas, & Bachmann, 2019). This would be consistent with geologic evidence of smaller eruption volumes. Reconciling the discrepancy between our inversion results and the geologic perspective would require more realistic geodetic source models for an mush system containing distinct high melt fraction bodies.

Gas solubility modeling using VolatileCalc (Newman & Lowenstern, 2002) constrained by carbon dioxide emissions and extruded volume give 4.4 wt% dissolved H_2O and 37 ppm dissolved CO_2 at 130 MPa, the pressure at the top of the magma chamber assumed at 5 km depth (Gerlach et al., 2008). This is consistent with inversion estimates of 3.34-4.65 wt% dissolved H_2O and 22.0-100.3 ppm dissolved CO_2. The same gas solubility modeling suggests a porosity $10.11-10.85\%$ at 130 MPa (Gerlach et al., 2008). At similar pressures, our inversion results give a porosity of $5.5-10.5\%$. There are some models with higher porosities at the conduit base (up to 20%), but these have shorter conduit lengths and their conduit base pressure is lower, allowing gas to exsolve and expand.

Melt inclusions in amphiboles and plagioclase suggest dissolved H_2O contents up to 3.6 wt%, however most are below 3 wt% which is considered low for the magma equilibration pressure of 130 MPa (Blundy et al., 2008; Pallister et al., 2008). This suggests that melt inclusions may have ruptured or crystallized during ascent and might not be representative of the actual dissolved water content in the chamber (Blundy et al., 2008; Pallister et al., 2008; ?, ?). Our inversions, which give dissolved water contents above 3 wt%, supports this interpretation.

The magma permeability scale k_c controls the balance between chamber volatile contents and observed dome porosity, because the distribution of k_c remains consistent across all four appraisals. This behavior is consistent with inversions using the steady-state version of this conduit flow model (Wong et al., 2017). However, Wong et al. (2017) found a tight constraint on $k_c \sim 10^{-12.3} - 10^{-10.5}$ m^2, while the distribution derived here finds lower k_c. We attribute this difference to the steady-state assumption as discussed in Section 4.3 of Wong and Segall (2019). Since each steady-state solution is independent, the solution adjusts to ensure that magma and gas flux into the region above the percolation threshold is sufficient to sustain gas escape. The magma column remains gas-rich even with extensive gas escape due to high permeability allowing extensive gas ascent. In time-dependent solutions, however, high magma permeability allows a large proportion of volatiles to be lost to the surroundings at early time to substantially decrease the amount of gas in the shallow conduit. This causes the eruption velocity to slow down drastically which is inconsistent with the extrusion volume time series. Therefore this high permeability constant is no longer preferred. Instead, an intermediate value that allows only moderate gas escape is preferred.

Laboratory measurements of permeability in the Mount St. Helens plug found vertical permeability of 10^{-14} m^2 in the margins and 10^{-15} m^2 in the core of the lava dome (Gaunt et al., 2014). Horizontal permeability was found to be 10^{-18} m^2 in the margins and 10^{-15} m^2 in the core (Gaunt et al., 2014). Our modeled permeability captures this range of values with few models having permeability greater than 10^{-14} m^2, although it does not account for the anisotropy observed in the experiments. Two-dimensional numerical models suggest that at shallow depths, gases tend to concentrate near the conduit margins which enhances gas escape (Collombet, 2009). This is corroborated by ring-shaped degassing observations at Santiaguito volcano in Guatemala (Bluth & Rose, 2004).

Furthermore, we do not consider the impact of crystals on gas percolation in equation 9. Experiments have shown that the presence of crystals can enhance bubble nucleation and control bubble size (Belien et al., 2010; Spina et al., 2016). Channelization of gas flow may occur at high crystal contents particularly in magmas with elongated crystals, leading to efficient gas migration (Oppenheimer et al., 2015; Spina et al., 2016). Higher-dimensional, pore-scale simulations better capture this spatially localized mode of degassing (Parmigiani et al., 2016; Degruyter et al., 2019). In contrast, this study focuses on the macro-scale impact of gas escape on extrusion flux, ground deformation and gas emissions, which are unable to resolve the spatial heterogeneity of gas flow.

Inversion results suggest a narrow conduit of radius $11.9 - 35.8$ m. Previous inversions with the steady-state conduit model used linear extrusion rates observed by remote cameras (Major et al., 2008) and extrusion flux to estimate the conduit radius, giving a best-fit radius of 148 m (Wong et al., 2017). Deformation was not included as a constraint in Wong et al. (2017). In this inversion, we omitted the linear extrusion rate as a constraint because it may only reflect the near-surface conduit geometry. Flaring conduit geometries have been seen in the rare cases where we have camera observations a few 100 meters into conduits (Lyons et al., 2016; Moussallam et al., 2016; Johnson et al., 2018). Mechanical modeling also shows that conduit collapse during explosive eruptions can create the flared geometry at the top (Macedonio et al., 1994; Mitchell, 2005; Aravena et al., 2017). Therefore including the linear extrusion rate would have biased results towards conduit radii larger than the average radius of the conduit.

Information from the amplitude and temporal evolution of observations provides the constraint on radius, as seen in sensitivity analyses of Wong and Segall (2019). When holding all other parameters constant, doubling conduit radius would increase the magma velocity and mass flow rate by 4 and 16 times respectively. The rate of pressure evolution, which is proportional to mass flow rate (equation 10), will also increase by 16 times. To maintain the same mass flow rate, we would need to reduce the chamber pressure, but this would cause the total extruded volume and radial displacements to decrease which would reduce the fit to observations. In addition, chamber pressure cannot decrease by 16 times, as it would cause the magma to be underpressured. Chamber volumes considered here could vary by that extent, however it would alter the relative magnitudes of extruded volume and radial displacements. The conduit radii of 11.9−35.8 m balance these competing effects to ensure fit to the data.

The smaller radius may also explain the higher pressure over magmastatic and the lower friction coefficient estimated here compared to the distribution obtained from the steady-state model. Previous inversions using the steady-state conduit model already estimated low f_0 (10^{-2}–$10^{-0.25}$), with the maximum *a posteriori* model having $f_0 = 0.46$ (Wong et al., 2017). The conduit model only resolves shear stress on the conduit walls $\tau_R = f(\sigma - p_{\text{hyd}})$, where the normal stress σ was assumed to be lithostatic and the pore pressure p_{hyd} was assumed to be hydrostatic. Decreasing σ by considering topographic or tectonic effects could result in higher estimated f_0. Elevated pore pressures due to gases escaping laterally and localizing on the conduit margins may also increase the estimated f_0. Even so, the f_0 estimated in this study are lower than in (Wong et al., 2017), suggesting that other reasons, such as the narrower conduit, must cause the low friction estimated in inversions using the time-dependent model. A narrower conduit has a higher ratio of surface area to cross-sectional area. To maintain the same flow rate, we would need to increase the driving force for flow, or reduce the viscous and/or frictional losses. The slight positive correlation between radius and the nominal friction coefficient (Figure 9) suggests that within the limited range of radii that fit the data, the friction coefficient is lower for narrower conduits. The weak relationship implies that other parameters trade off with friction coefficient. Of course, inaccuracies in the model for magma viscosity will trade off with estimates of the frictional resistance. Viscosity models with reduced dependence on the crystal fraction compared to the Costa (2005) model would reduce viscous losses, and therefore require greater frictional losses and hence a a higher friction coefficient to achieve the same mass flow rate.

5 Conclusion

In this study, we applied a simple physics-based model to estimate critical properties of the magmatic system at Mount St. Helens based on diverse time series data from the 2004-2008 eruption. The model takes into account pressure-dependent crystallization, volatile exsolution and gas escape during magma ascent. These processes cause magma flowing viscously at depth to transition to solid plug sliding at shallow depth, ultimately extruding a dome in the crater. To constrain important parameters in the model, we jointly apply extruded volume, continuous and campaign GPS positions and carbon dioxide emissions time series from the eruption in an inversion using the neighborhood algorithm (Sambridge, 1999b, 1999a).

Key findings of the inversion include:

1. We are able to find models that fit the extruded volume, ground deformation and carbon dioxide emissions from the 2004-2008 eruption at Mount St. Helens. In particular, the best-fit model approximately captures the rapid decay in JRO1 radial displacement while maintaining satisfactory fits to the other datasets, which previous studies were unable to replicate.
2. The data prefer elongate chambers with aspect ratios $0.13-0.55$, located at $9.00-17.2$ km depth with chamber volumes between $64.1-256$ km^3. These chamber volumes suggest that solutions to the full time-dependent governing equations is needed to model the temporal evolution of the eruption. Volume lost from the chamber is $20-66$ million m^3.
3. The top of the chamber has total (dissolved and exsolved) water contents of $4.99-6.44$ wt% and carbon dioxide contents of $1560-3891$ ppm. At 130 MPa, which is the top of the magma chamber inferred from plagioclase phase equilibrium, this corresponds to a porosity of 5.5-10%.
4. Excess exsolved volatiles to escape the system vertically through the conduit and laterally through the conduit walls. The magma permeability scale is well-constrained by the porosity of dome rock.
5. Compared to previous inversions using the steady-state conduit model (Wong et al., 2017), this inversion using the time-dependent model suggests a lower magma permeability scale because of differences in the mechanism for gas escape in steady-state and time-dependent conduit flow models. In addition, a narrower conduit of radius $11.9-35.8$ m is preferred. This may account for the higher pressure over magmastatic ($13.1-55.5$ MPa) and lower conduit wall friction coefficients ($0.014-0.057$ at the reference velocity $v = v_r = 10^{-5}$ m/s). A weaker dependence of viscosity on crystal fraction would allow larger friction coefficients.

Acknowledgments

This study was supported by the National Science Foundation (NSF) [10.13039/100000001] EAR-1358607. Code used and developed in this study are available here: conduit model (`http://doi.org/10.5281/zenodo.3969094`), parameter estimation (`http://doi.org/10.5281/zenodo.3969103`), inversions for Mount St. Helens (`http://doi.org/10.5281/zenodo.3969090`), inversion results files (`http://doi.org/10.5281/zenodo.3969105`). Data from the Mount St. Helens eruption are available from Schilling et al. (2008), Lisowski et al. (2008), Gerlach et al. (2008) and Dzurisin et al. (2015), as well as the USGS Pacific Northwest GPS Network (`https://earthquake.usgs.gov/monitoring/gps/Pacific_Northwest`). We are grateful to Michael Lisowski for help in processing the GPS data.

References

Albino, F., Pinel, V., Massol, H., & Collombet, M. (2011). Conditions for detection of ground deformation induced by conduit flow and evolution. *Journal of Geophysical Research: Solid Earth*, *116*(6), 1–18. doi: 10.1029/2010JB007871

Amoruso, A., & Crescentini, L. (2009). Shape and volume change of pressurized ellipsoidal cavities from deformation and seismic data. *Journal of Geophysical Research: Solid Earth*, *114*(2), 1–8. doi: 10.1029/2008JB005946

Anderson, K., Lisowski, M., & Segall, P. (2010). Cyclic ground tilt associated with the 2004-2008 eruption of Mount St. Helens. *Journal of Geophysical Research: Solid Earth*, *115*(11), 1–29. doi: 10.1029/2009JB007102

Anderson, K., & Segall, P. (2011). Physics-based models of ground deformation and extrusion rate at effusively erupting volcanoes. *Journal of Geophysical Research: Solid Earth*, *116*(7), 1–20. doi: 10.1029/2010JB007939

Anderson, K., & Segall, P. (2013). Bayesian inversion of data from effusive volcanic eruptions using physics-based models: Application to Mount St. Helens 2004-2008. *Journal of Geophysical Research: Solid Earth*, *118*(5), 2017–2037. doi: 10.1002/jgrb.50169

Aravena, A., de'Michieli Vitturi, M., Cioni, R., & Neri, A. (2017). Stability of volcanic conduits during explosive eruptions. *Journal of Volcanology and Geothermal Research*. Retrieved from http://linkinghub.elsevier.com/retrieve/pii/S0377027317301427 doi: 10.1016/j.jvolgeores.2017.05.003

Belien, I. B., Cashman, K. V., & Rempel, A. W. (2010). Gas accumulation in particle-rich suspensions and implications for bubble populations in crystal-rich magma. *Earth and Planetary Science Letters*, *297*(1-2), 133–140. Retrieved from http://dx.doi.org/10.1016/j.epsl.2010.06.014 doi: 10.1016/j.epsl.2010.06.014

Blower, J. (2001). Factors controlling permeability-porosity relationships in magma. *Bulletin of Volcanology*, *63*, 497–504. doi: 10.1007/s004450100172

Blundy, J., Cashman, K. V., & Berlo, K. (2008). Evolving magma storage conditions beneath Mount St. Helens inferred from chemical variations in melt inclusions from the 1980-1986 and current (2004-2006) eruptions. *A Volcano Rekindled: The Renewed Eruption of Mount St. Helens 2004-2006, U.S. Geological Survey Professional Paper 1750*, 755–790. Retrieved from http://www.scopus.com/inward/record.url?eid=2-s2.0-84864213506{\&}partnerID=40{\&}md5=882e27194e3279f6c7076734494e88d8

Bluth, G. J., & Rose, W. I. (2004). Observations of eruptive activity at Santiaguito volcano, Guatemala. *Journal of Volcanology and Geothermal Research*, *136*(3-4), 297–302. doi: 10.1016/j.jvolgeores.2004.06.001

Carey, S., Gardner, J., & Sigurdsson, H. (1995). The intensity and magnitude of Holocene plinian eruptions from Mount St. Helens volcano. *Journal of Volcanology and Geothermal Research*, *66*(1-4), 185–202. doi: 10.1016/0377-0273(94)00059-P

Caricchi, L., Burlini, L., Ulmer, P., Gerya, T., Vassalli, M., & Papale, P. (2007). Non-Newtonian rheology of crystal-bearing magmas and implications for magma ascent dynamics. *Earth and Planetary Science Letters*, *264*(3-4), 402–419. doi: 10.1016/j.epsl.2007.09.032

Cashman, K. V., Thornber, C., & Pallister, J. S. (2008). From Dome to Dust: Shallow Crystallization and Fragmentation of Conduit Magma During the 2004-2006 Dome Extrusion of Mount St . Helens, Washington. *A Volcano Rekindled: The Renewed Eruption of Mount St. Helens 2004-2006, U.S. Geological Survey Professional Paper 1750*, 387–413. Retrieved from http://cat.inist.fr/?aModele=afficheN{\&}cpsidt=22527815

Clynne, M. A., Calvert, A. T., Wolfe, E. W., Evarts, R. C., Fleck, R. J., & Lanphere, M. A. (2008). The pleistocene eruptive history of Mount St. Helens, Washington, from 300,000 to 12,800 years before present. *US Geological Survey Professional Paper*(1750), 593–628. doi: 10.3133/pp175028

Collombet, M. (2009). Two-dimensional gas loss for silicic magma flows: Toward more realistic numerical models. *Geophysical Journal International*, *177*(1), 309–318. doi: 10.1111/j.1365-246X.2008.04086.x

Costa, A. (2005). Viscosity of high crystal content melts: Dependence on solid fraction. *Geophysical Research Letters*, *32*(22), 1–5. doi: 10.1029/2005GL024303

Crowell, B. W., Bock, Y., & Liu, Z. (2016). Single-station automated detection of transient deformation in GPS time series with the relative strength index: A case study of Cascadian slow slip. *Journal of Geophysical Research: Solid Earth*, *121*(12), 9077–9094. doi: 10.1002/2016JB013542

De' Michieli Vitturi, M., Clarke, A. B., Neri, A., & Voight, B. (2013). Extrusion cycles during dome-building eruptions. *Earth and Planetary Science Letters*, *371-372*, 37–48. Retrieved from http://dx.doi.org/10.1016/j.epsl.2013.03.037 doi: 10.1016/j.epsl.2013.03.037

Degruyter, W., Parmigiani, A., Huber, C., & Bachmann, O. (2019, feb). How do volatiles escape their shallow magmatic hearth? *Philosophical Transactions of the Royal Society A: Mathematical, Physical and Engineering Sciences*, *377*(2139). Retrieved from `http://www.royalsocietypublishing.org/doi/10.1098/rsta.2018.0017` doi: 10.1098/rsta.2018.0017

Denlinger, R. P., & Hoblitt, R. P. (1999). Cyclic eruptive behavior of silicic volcanoes. *Geology*, *27*(5), 459–462. doi: 10.1130/0091-7613(1999)027⟨0459

Dzurisin, D., Moran, S. C., Lisowski, M., Schilling, S. P., Anderson, K. R., & Werner, C. (2015). The 2004-2008 dome-building eruption at Mount St. Helens, Washington: epilogue. *Bulletin of Volcanology*, *77*(10), 89. Retrieved from `http://link.springer.com/10.1007/s00445-015-0973-4` doi: 10.1007/s00445-015-0973-4

Fukushima, Y., Cayol, V., & Durand, P. (2005). Finding realistic dike models from interferometric synthetic aperture radar data: The February 2000 eruption at Piton de la Fournaise. *Journal of Geophysical Research: Solid Earth*, *110*(3), 1–15. doi: 10.1029/2004JB003268

Gaunt, H. E., Sammonds, P. R., Meredith, P. G., Smith, R., & Pallister, J. S. (2014). Pathways for degassing during the lava dome eruption of Mount St. Helens 2004-2008. *Geology*, *42*(11), 947–950. Retrieved from `http://geology.gsapubs.org/cgi/doi/10.1130/G35940.1` doi: 10.1130/G35940.1

Gerlach, T. M., Mcgee, K. A., & Doukas, M. P. (2008). Emission Rates of CO2, SO2, and H2S, Scrubbing, and Preeruption Excess Volatiles at Mount St. Helens, 2004-2005. *A Volcano Rekindled: The Renewed Eruption of Mount St. Helens 2004-2006, U.S. Geological Survey Professional Paper 1750*, 543–571.

Gonnermann, H. M., & Manga, M. (2007). The Fluid Mechanics Inside a Volcano. *Annual Review of Fluid Mechanics*, *39*, 321–356. doi: 10.1146/annurev.fluid.39.050905.110207

Iverson, R. M. (2008). Dynamics of Seismogenic Volcanic Extrusion Resisted by a Solid Surface Plug, Mount St. Helens, 2004-2005. *A Volcano Rekindled: The Renewed Eruption of Mount St. Helens 2004-2006, U.S. Geological Survey Professional Paper 1750*, 425–460.

Jaupart, C., & Allègre, C. J. (1991). Gas content, eruption rate and instabilities of eruption regime in silicic volcanoes. *Earth and Planetary Science Letters*, *102*(3-4), 413–429. doi: 10.1016/0012-821X(91)90032-D

Johnson, J. B., Watson, L. M., Palma, J. L., Dunham, E. M., & Anderson, J. F. (2018). Forecasting the Eruption of an Open-Vent Volcano Using Resonant Infrasound Tones. *Geophysical Research Letters*, *45*(5), 2213–2220. doi: 10.1002/2017GL076506

Kawaguchi, R., & Nishimura, T. (2015). Numerical investigation of temporal changes in volcanic deformation caused by a gas slug ascent in the conduit. *Journal of Volcanology and Geothermal Research*, *302*, 1–10. Retrieved from `http://dx.doi.org/10.1016/j.jvolgeores.2015.06.002` doi: 10.1016/j.jvolgeores.2015.06.002

Kiser, E., Palomeras, I., Levander, A., Zelt, C., Harder, S., Schmandt, B., ... Ulberg, C. (2016). Magma reservoirs from the upper crust to the Moho inferred from high-resolution Vp and Vs models beneath Mount St. Helens, Washington State, USA. *Geology*, *44*(6), G37591.1. Retrieved from `http://geology.gsapubs.org/lookup/doi/10.1130/G37591.1` doi: 10.1130/G37591.1

Klug, C., & Cashman, K. V. (1996). Permeability development in vesiculating magmas: implications for fragmentation. *Bulletin of Volcanology*, *58*, 87–100. doi: 10.1007/s004450050128

Kozono, T., & Koyaguchi, T. (2012). Effects of gas escape and crystallization on the complexity of conduit flow dynamics during lava dome eruptions. *Journal of Geophysical Research: Solid Earth*, *117*(March), 1–18. doi:

10.1029/2012JB009343

Langbein, J. (2004). Noise in two-color electronic distance meter measurements revisited. *Journal of Geophysical Research: Solid Earth*, *109*(4), 1–16. doi: 10.1029/2003JB002819

Leeman, W. P., & Smith, D. R. (2018). The role of magma mixing, identification of mafic magma inputs, and structure of the underlying magmatic system at Mount St. Helens. *American Mineralogist*, *103*(12), 1925–1944. doi: 10.2138/am-2018-6555

Lisowski, M., Dzurisin, D., Denlinger, R. P., & Iwatsubo, E. Y. (2008). Analysis of GPS-Measured Deformation Associated with the 2004-2006 Dome-Building Eruption of Mount St. Helens, Washington. *A Volcano Rekindled: The Renewed Eruption of Mount St. Helens 2004-2006, U.S. Geological Survey Professional Paper 1750*, 301–333.

Liu, Y., Zhang, Y., & Behrens, H. (2005). Solubility of H2O in rhyolitic melts at low pressures and a new empirical model for mixed H2O-CO2 solubility in rhyolitic melts. *Journal of Volcanology and Geothermal Research*, *143*(1-3), 219–235. doi: 10.1016/j.jvolgeores.2004.09.019

Llewellin, E. W., & Manga, M. (2005). Bubble suspension rheology and implications for conduit flow. *Journal of Volcanology and Geothermal Research*, *143*(1-3), 205–217. doi: 10.1016/j.jvolgeores.2004.09.018

Lyons, J. J., Haney, M. M., Werner, C., Kelly, P., Patrick, M., Kern, C., & Trusdell, F. (2016, jan). Long period seismicity and very long period infrasound driven by shallow magmatic degassing at Mount Pagan, Mariana Islands. *Journal of Geophysical Research: Solid Earth*, *121*(1), 188–209. Retrieved from `http://doi.wiley.com/10.1002/2015JB012490` doi: 10.1002/2015JB012490

Macedonio, G., Dobran, F., & Neri, A. (1994, jan). Erosion processes in volcanic conduits and application to the AD 79 eruption of Vesuvius. *Earth and Planetary Science Letters*, *121*(1-2), 137–152. Retrieved from `https://linkinghub.elsevier.com/retrieve/pii/0012821X9490037X` doi: 10.1016/0012-821X(94)90037-X

Major, J. J., Kingsbury, C. G., Poland, M. P., & Lahusen, R. G. (2008). Extrusion Rate of the Mount St. Helens Lava Dome Estimated from Terrestrial Imagery, November 2004December 2005. *A Volcano Rekindled: The Renewed Eruption of Mount St. Helens 2004-2006, U.S. Geological Survey Professional Paper 1750*, 237–255.

Manning, C. E., & Ingebritsen, S. E. (1999). Permeability of the continental crust: Implications of geothermal data and metamorphic systems. *Reviews of Geophysics*, *37*(1), 127–150.

Mao, A., Harrison, C. G. A., & Dixon, T. H. (1999, feb). Noise in GPS coordinate time series. *Journal of Geophysical Research: Solid Earth*, *104*(B2), 2797–2816. Retrieved from `http://doi.wiley.com/10.1029/1998JB900033` doi: 10.1029/1998JB900033

Mastin, L. G. (2002). Insights into volcanic conduit flow from an open-source numerical model. *Geochemistry, Geophysics, Geosystems*, *3*(7), 1–18.

Mastin, L. G., Lisowski, M., Roeloffs, E., & Beeler, N. (2009). Improved constraints on the estimated size and volatile content of the Mount St. Helens magma system from the 2004-2008 history of dome growth and deformation. *Geophysical Research Letters*, *36*, 1–4. doi: 10.1029/2009GL039863

Melnik, O., & Sparks, R. S. J. (2005). Controls on conduit magma flow dynamics during lava dome building eruptions. *Journal of Geophysical Research B: Solid Earth*, *110*(2), 1–21. doi: 10.1029/2004JB003183

Mitchell, K. L. (2005). Coupled conduit flow and shape in explosive volcanic eruptions. *Journal of Volcanology and Geothermal Research*, *143*(1-3), 187–203. doi: 10.1016/j.jvolgeores.2004.09.017

Moran, S. C., Malone, S. D., Qamar, a. I., Thelen, W. a., Wright, a. K., & Caplan-Auerbach, J. (2008). Seismicity Associated with Renewed Dome Building at Mount St. Helens, 2004-2005. *A Volcano Rekindled: The Renewed Eruption of Mount St. Helens 2004-2006, U.S. Geological Survey Professional Paper 1750*, 27–60. Retrieved from http://cat.inist.fr/?aModele=afficheN{\&}cpsidt=22527798{\%}5Cnpapers2://publication/uuid/B8CC1216-2240-4CDA-B943-F693FBD90597

Moussallam, Y., Bani, P., Curtis, A., Barnie, T., Moussallam, M., Peters, N., ... Cardona, C. (2016). Sustaining persistent lava lakes: Observations from high-resolution gas measurements at Villarrica volcano, Chile. *Earth and Planetary Science Letters*, *454*, 237–247. Retrieved from http://dx.doi.org/10.1016/j.epsl.2016.09.012 doi: 10.1016/j.epsl.2016.09.012

Neuberg, J. W., Collinson, A. S., Mothes, P. A., C. Ruiz, M., & Aguaiza, S. (2018). Understanding cyclic seismicity and ground deformation patterns at volcanoes: Intriguing lessons from Tungurahua volcano, Ecuador. *Earth and Planetary Science Letters*, *482*, 193–200. Retrieved from https://doi.org/10.1016/j.epsl.2017.10.050 doi: 10.1016/j.epsl.2017.10.050

Newman, S., & Lowenstern, J. B. (2002). Volatile Calc : a silicate melt H2O CO2 solution model written in Visual Basic for excel. *Computers & Geosciences*, *28*, 597–604. doi: doi:10.1016/S0098-3004(01)00081-4

Oppenheimer, J., Rust, A. C., Cashman, K. V., & Sandnes, B. (2015). Gas migration regimes and outgassing in particle-rich suspensions. *Frontiers in Physics*, *3*(August), 1–13. Retrieved from http://journal.frontiersin.org/Article/10.3389/fphy.2015.00060/abstract doi: 10.3389/fphy.2015.00060

Palano, M., Guarrera, E., & Mattia, M. (2012). GPS ground deformation patterns at Mount St. Helens (Washington, USA) from 2004 to 2010. *Terra Nova*, *24*(2), 148–155. doi: 10.1111/j.1365-3121.2011.01049.x

Pallister, J. S., Clynne, M. A., Wright, H. M., Eaton, A. R. V., Vallance, J. W., Sherrod, D. R., & Kokelaar, B. P. (2017). Field-trip guide to Mount St. Helens, Washington - An overview of the eruptive history and petrology, tephra deposits, 1980 pyroclastic density current deposits, and the crater. *Scientific Investigations Report*, 23. Retrieved from https://pubs.er.usgs.gov/publication/sir20175022D doi: 10.3133/sir20175022d

Pallister, J. S., Thornber, C. R., Cashman, K. V., Clynne, M. a., Lowers, H. a., Mandeville, C. W., ... Meeker, G. P. (2008). Petrology of the 2004-2006 Mount St. Helens Lava Dome – Implications for Magmatic Plumbing and Eruption Triggering. *A Volcano Rekindled: The Renewed Eruption of Mount St. Helens 2004-2006, U.S. Geological Survey Professional Paper 1750*, 647–702.

Papale, P. (2001). Dynamics of magma flow in volcanic conduits with variable fragmentation efficiency and nonequilibrium pumice degassing. *Journal of Geophysical Research: Solid Earth*, *106*(B6), 11043–11065. Retrieved from http://doi.wiley.com/10.1029/2000JB900428 doi: 10.1029/2000JB900428

Parmigiani, A., Faroughi, S., Huber, C., Bachmann, O., & Su, Y. (2016). Bubble accumulation and its role in the evolution of magma reservoirs in the upper crust. *Nature*, *532*(7600), 492–495. doi: 10.1038/nature17401

Plank, T., Kelley, K. a., Zimmer, M. M., Hauri, E. H., & Wallace, P. J. (2013). Why do mafic arc magmas contain ~4wt% water on average? *Earth and Planetary Science Letters*, *364*, 168–179. Retrieved from http://dx.doi.org/10.1016/j.epsl.2012.11.044 doi: 10.1016/j.epsl.2012.11.044

Pritchard, M. E., & Simons, M. (2002). A satellite geodetic survey of large-scale deformation of volcanic centres in the central Andes. *Nature*, *418*(6894), 167–171. doi: 10.1038/nature00872

Rice, J. R., Lapusta, N., & Ranjith, K. (2001). Rate and state dependent friction and the stability of sliding between elastically deformable solids. *Journal of the Mechanics and Physics of Solids*, *49*(9), 1865–1898. doi: 10.1016/S0022-5096(01)00042-4

Saar, M. O., & Manga, M. (1999). Permeability-porosity relationship in vesicular basalts. *Geophysical Research Letters*, *26*(1), 111–114. doi: 10.1029/1998GL900256

Sambridge, M. (1999a). Geophysical inversion with a neighborhood algorithm - II. Appraising the ensemble. *Geophysical Journal International*, *138*, 727–746.

Sambridge, M. (1999b). Geophysical inversion with a neighbourhood algorithm - I. Searching a parameter space. *Geophysical Journal International*, *138*, 479–494.

Scandone, R., & Malone, S. D. (1985). Magma supply, magma discharge and readjustment of the feeding system of Mount St. Helens during 1980. *Journal of Volcanology and Geothermal Research*, *23*(3-4), 239–262. doi: 10.1016/0377-0273(85)90036-8

Schilling, S. P., Thompson, R., Messerich, J., & Iwatsubo, E. Y. (2008). Use of Digital Aerophotogrammetry to Determine Rates of Lava Dome Growth, Mount St. Helens, Washington, 2004-2005. *A Volcano Rekindled: The Renewed Eruption of Mount St. Helens 2004-2006, U.S. Geological Survey Professional Paper 1750*, 145–167.

Schneider, A., Rempel, A. W., & Cashman, K. V. (2012). Conduit degassing and thermal controls on eruption styles at Mount St. Helens. *Earth and Planetary Science Letters*, *357-358*, 347–354. Retrieved from `http://dx.doi.org/10.1016/j.epsl.2012.09.045` doi: 10.1016/j.epsl.2012.09.045

Scott, W. E., Sherrod, D. R., & Gardner, C. A. (2008). Overview of the 2004 to 2006, and Continuing, Eruption of Mount St. Helens, Washington. *A Volcano Rekindled: The Renewed Eruption of Mount St. Helens, 2004-2006: US Geological Survey Professional Paper 1750*(October 2004), 3–22.

Segall, P. (2013). Volcano deformation and eruption forecasting. *Geological Society, London, Special Publications*, *380*, 85–106. Retrieved from `http://sp.lyellcollection.org/cgi/doi/10.1144/SP380.4` doi: 10.1144/SP380.4

Smith, R., Sammonds, P. R., Tuffen, H., & Meredith, P. G. (2011). Evolution of the mechanics of the 2004-2008 Mt. St. Helens lava dome with time and temperature. *Earth and Planetary Science Letters*, *307*(1-2), 191–200. Retrieved from `http://dx.doi.org/10.1016/j.epsl.2011.04.044` doi: 10.1016/j.epsl.2011.04.044

Spina, L., Cimarelli, C., Scheu, B., Di Genova, D., & Dingwell, D. B. (2016). On the slow decompressive response of volatile- and crystal-bearing magmas: An analogue experimental investigation. *Earth and Planetary Science Letters*, *433*, 44–53. Retrieved from `http://dx.doi.org/10.1016/j.epsl.2015.10.029` doi: 10.1016/j.epsl.2015.10.029

Thornber, C. R., Pallister, J. S., Rowe, M. C., Mcconnell, S., Herriott, T. M., Eckberg, A., ... Knaack, C. M. (2008). *Catalog of Mount St . Helens 2004 2007 Dome Samples with Major- and Trace-element Chemistry: U.S. Geological Survey Open-File Report 2008-1130* (Tech. Rep.). U.S. Geological Survey. Retrieved from `http://pubs.usgs.gov/of/2008/1130/`

Vallance, J., Schneider, D., & Schilling, S. (2008). Growth of the 2004-2006 Lava-Dome Complex at Mount St. Helens, Washington. *A Volcano Rekindled: The Renewed Eruption of Mount St. Helens 2004-2006, U.S. Geological Survey Professional Paper 1750*, 169–208.

Wanke, M., Clynne, M. A., von Quadt, A., Vennemann, T. W., & Bachmann, O. (2019). Geochemical and petrological diversity of mafic magmas from Mount St. Helens. *Contributions to Mineralogy and Petrology*, *174*(1), 1–25. Retrieved from `http://dx.doi.org/10.1007/s00410-018-1544-4` doi:

10.1007/s00410-018-1544-4

Wanke, M., Karakas, O., & Bachmann, O. (2019). The genesis of arc dacites: the case of Mount St. Helens, WA. *Contributions to Mineralogy and Petrology*, *174*(1), 1–14. Retrieved from http://dx.doi.org/10.1007/s00410-018-1542-6 doi: 10.1007/s00410-018-1542-6

Whittington, A. G., Hellwig, B. M., Behrens, H., Joachim, B., Stechern, A., & Vetere, F. (2009). The viscosity of hydrous dacitic liquids: Implications for the rheology of evolving silicic magmas. *Bulletin of Volcanology*, *71*(2), 185–199. doi: 10.1007/s00445-008-0217-y

Williams, S. D. (2008). CATS: GPS coordinate time series analysis software. *GPS Solutions*, *12*(2), 147–153. doi: 10.1007/s10291-007-0086-4

Wong, Y.-Q., & Segall, P. (2019, nov). Numerical Analysis of Time-Dependent Conduit Magma Flow in Dome-Forming Eruptions With Application to Mount St. Helens 2004-2008. *Journal of Geophysical Research: Solid Earth*, *124*(11), 11251–11273. Retrieved from https://onlinelibrary.wiley.com/doi/abs/10.1029/2019JB017585 doi: 10.1029/2019JB017585

Wong, Y.-Q., Segall, P., Bradley, A., & Anderson, K. (2017, oct). Constraining the Magmatic System at Mount St. Helens (2004-2008) Using Bayesian Inversion With Physics-Based Models Including Gas Escape and Crystallization. *Journal of Geophysical Research: Solid Earth*, *122*(10), 7789–7812. Retrieved from http://doi.wiley.com/10.1002/2017JB014343 doi: 10.1002/2017JB014343

Yang, X.-M., Davis, P. M., & Dieterich, J. H. (1988, may). Deformation from inflation of a dipping finite prolate spheroid in an elastic half-space as a model for volcanic stressing. *Journal of Geophysical Research*, *93*(B5), 4249. Retrieved from http://doi.wiley.com/10.1029/JB093iB05p04249 doi: 10.1029/JB093iB05p04249